leech may provide a system in which to resolve this important question.

References and Notes

1. P. W. Glimcher, *Decisions, Uncertainty and the Brain: The Science of Neuroeconomics* (MIT Press, Cambridge, MA, 2003).
2. M. N. Shadlen, W. T. Newsome, *Proc. Natl. Acad. Sci. U.S.A.* **93**, 628 (1996).
3. P. W. Glimcher, *Trends Neurosci.* **24**, 654 (2001).
4. J. D. Schall, *Curr. Biol.* **10**, R404 (2000).
5. M. N. Shadlen, W. T. Newsome, *J. Neurophysiol.* **86**, 1916 (2001).
6. J. I. Gold, M. N. Shadlen, *Nature* **404**, 390 (2000).
7. M. L. Platt, P. W. Glimcher, *Nature* **400**, 233 (1999).
8. R. Romo, E. Salinas, *Annu. Rev. Neurosci.* **24**, 107 (2001).
9. M. P. Kovac, W. J. Davis, *Science* **198**, 632 (1977).
10. M. P. Kovac, W. J. Davis, *J. Neurophysiol.* **43**, 469 (1980).
11. T. Esch, W. B. Kristan Jr., *Integr. Comp. Biol.* **42**, 716 (2002).
12. I. R. Popescu, W. N. Frost, *J. Neurosci.* **22**, 1985 (2002).
13. W. B. Kristan Jr., R. L. Calabrese, *J. Exp. Biol.* **65**, 643 (1976).
14. F. J. Eisenhart, T. W. Cacciatore, W. B. Kristan Jr., *J. Comp. Physiol.* **A186**, 631 (2000).
15. W. B. Kristan Jr., *J. Exp. Biol.* **96**, 161 (1982).
16. W. B. Kristan Jr., S. J. McGirr, G. V. Simpson, *J. Exp. Biol.* **96**, 143 (1982).
17. T. W. Cacciatore, R. Rozenshteyn, W. B. Kristan Jr., *J. Neurosci.* **20**, 1643 (2000).
18. J. D. Schall, *Nature Rev. Neurosci.* **2**, 33 (2001).
19. J. C. Weeks, W. B. Kristan Jr., *J. Exp. Biol.* **77**, 71 (1978).
20. P. D. Brodfuehrer, A. Burns, *Neurobiol. Learn. Mem.* **63**, 192 (1995).
21. T. Esch, K. A. Mesce, W. B. Kristan Jr., *J. Neurosci.* **22**, 11045 (2002).
22. B. K. Shaw, W. B. Kristan Jr., *J. Neurosci.* **17**, 786 (1997).
23. M. Zochowski, L. B. Cohen, G. Fuhrmann, D. Kleinfeld, *J. Neurosci.* **20**, 8485 (2000).
24. J. E. González, K. Oades, Y. Leychkis, A. Harootunian, P. A. Negulescu, *Drug Discov. Today* **4**, 431 (1999).
25. T. W. Cacciatore *et al.*, *Neuron* **23**, 449 (1999).
26. A. L. Taylor, G. W. Cottrell, D. Kleinfeld, W. B. Kristan Jr., *J. Neurosci.* **23**, 11402 (2003).
27. K. J. Muller, J. G. Nicholls, G. S. Stent, *Neurobiology of the Leech* (Cold Spring Harbor, New York, 1981).
28. Materials and methods are available as supporting material on *Science* Online.
29. D. Kaplan, L. Glass, *Understanding Nonlinear Dynamics* (Springer-Verlag, New York, 1995).
30. H. Abarbanel, *Analysis of Observed Chaotic Data* (Springer-Verlag, New York, 1996).
31. D. S. Broomhead, G. P. King, *Phys. D* **20**, 217 (1986).
32. D. S. Broomhead, R. Jones, G. P. King, *J. Phys. A* **20**, 563 (1987).
33. LDA seeks a line in the multidimensional phase space of a system such that grouped data points projected onto the line are maximally separated (i.e., the distributions of swimming versus crawling data points along the line are maximally separated). The slope of this line indicates the relative contribution of each of the variables to this separation. The goal is to find the time at which the swimming and crawling data projected onto a linear discriminant are significantly separated. This technique is susceptible to overfitting when applied in a high-dimensional space with a limited amount of data. To overcome this problem, one may either increase the number of samples or decrease the dimensionality of the system. Phototoxicity limits the amount of data we can collect, so we instead used PCA to reduce the dimensionality of our data sets.
34. PCA rotates the axes of our *N*-dimensional data (where *N* is the number of neurons) so that the first few axes point in the directions of maximal covariance. These new directions are the PCs. A neuron with very different activity between swimming and crawling trials will have a large variance across trials. This neuron would then contribute strongly to one of the first few PCs.
35. R. O. Duda, P. E. Hart, D. G. Stork, *Pattern Classification* (Wiley, New York, ed. 2, 2000).
36. K. Mardia, J. Kent, J. Bibby, *Multivariate Analysis* (Academic Press, San Diego, CA, 1980).
37. The combination of PCA and LDA found linear combinations of neurons that could discriminate the behaviors earlier than any single neuron. Although each of the PCs we discarded did not explain much of the total variance, it is possible that we lost discrimination information by not using them. Thus, although the linear discriminants we found performed well (i.e., discriminated at an early t_{LDA}), an earlier t_{LDA} may have been found had we been able to use all of the PCs. This illustrates the inherent tradeoff between the dimensionality of a system and the amount of data required to adequately sample a high-dimensional space.
38. J. Weeks, *J. Comp. Physiol.* **148**, 265 (1982).
39. W. B. Kristan Jr., B. K. Shaw, *Curr. Opin. Neurobiol.* **7**, 826 (1997).
40. We thank J. E. Gonzalez and R. Y. Tsien for assistance with the FRET voltage-sensitive dyes; Panvera LLC for supplying the dyes gratis; C. Schaffer for assistance with designing the wavelength-switching device; J. Shlens, A. L. Taylor, S. B. Mehta, and E. Thomson for valuable discussions; and H. J. Chiel, M. B. Feller, D. Kleinfeld, and T. J. Sejnowksi for helpful comments and suggestions on an earlier version of this manuscript. Supported by a La Jolla Interfaces in Science Predoctoral Fellowship, funded by the Burroughs Wellcome Fund (K.L.B.); a NSF Integrative Graduate Education and Research Traineeship (IGERT) training grant (K.L.B.); NIH research grants nos. MH43396 (W.B.K.) and NS40110 (H.D.I.A); U.S. Department of Energy grant no. DE-FG03-90ER14138 (H.D.I.A); NSF research grant no. PHY0097134 (H.D.I.A); and the Office of Naval Research, contract no. N00014-00-1-0181 (H.D.I.A).

REPORTS

Nodal Quasiparticles and Antinodal Charge Ordering in Ca$_{2-x}$Na$_x$CuO$_2$Cl$_2$

Kyle M. Shen,[1] F. Ronning,[1]* D. H. Lu,[1] F. Baumberger,[1]
N. J. C. Ingle,[1] W. S. Lee,[1] W. Meevasana,[1] Y. Kohsaka,[2]
M. Azuma,[3] M. Takano,[3] H. Takagi,[2,4] Z.-X. Shen[1]†

Understanding the role of competing states in the cuprates is essential for developing a theory for high-temperature superconductivity. We report angle-resolved photoemission spectroscopy experiments which probe the $4a_0 \times 4a_0$ charge-ordered state discovered by scanning tunneling microscopy in the lightly doped cuprate superconductor Ca$_{2-x}$Na$_x$CuO$_2$Cl$_2$. Our measurements reveal a marked dichotomy between the real- and momentum-space probes, for which charge ordering is emphasized in the tunneling measurements and photoemission is most sensitive to excitations near the node of the *d*-wave superconducting gap. These results emphasize the importance of momentum anisotropy in determining the complex electronic properties of the cuprates and places strong constraints on theoretical models of the charge-ordered state.

To explain the mechanism of high-temperature superconductivity, it is necessary to understand how the parent Mott insulator, characterized by very strong electron-electron repulsion, can evolve into a high–transition temperature (T_c) superconductor upon the addition of a relatively small number of carriers. In the intervening region between the Mott insulator and high-T_c superconductor, the so-called "pseudogap" regime, highly anomalous physical properties have been observed (*1*). Many attempts to explain these unusual properties have centered around the possibility of competing orders, such as orbital currents (*2*), nanoscale charge ordering (*3*, *4*), or electronic phase separation (*5*). The particular importance of charge ordering has recently been underscored by the discovery of a distinct real-space pattern of $4a_0 \times 4a_0$ two-dimensional charge ordering (2DCO) in Ca$_{2-x}$Na$_x$CuO$_2$Cl$_2$ (Na-CCOC) by scanning tunneling microscopy (STM) (*6*). Angle-resolved photoemission spectroscopy (ARPES) can provide crucial

[1]Departments of Applied Physics, Physics, and Stanford Synchrotron Laboratory, Stanford University, Stanford, CA 94305, USA. [2]Department of Advanced Materials Science, University of Tokyo, Kashiwa, Chiba 277–8561, Japan. [3]Institute for Chemical Research, Kyoto University, Uji, Kyoto 611–0011, Japan. [4]RIKEN, The Institute for Physical and Chemical Research, Wako 351–0198, Japan.

*Present address: Los Alamos National Laboratory, Los Alamos, NM 87545, USA.
†To whom correspondence should be addressed. E-mail: zxshen@stanford.edu

901

insights into the microscopic nature of this 2DCO and its relationship to the single-particle excitations in **k**-space. We performed ARPES studies of Na-CCOC (x = 0.05, 0.10, and 0.12), allowing us to combine information from the complementary real- and **k**-space electronic probes. Our results reveal a strong momentum anisotropy, in which the 2DCO is associated with strongly suppressed anti-nodal electronic states that have a nesting wave vector of $|\mathbf{q}| \sim 2\pi/4a_0$, whereas the nodal states dominate the low-energy spectral weight in **k**-space.

ARPES measurements were performed at Beamline 5-4 of the Stanford Synchrotron Radiation Laboratory with the use of single crystals with typical dimensions of $1 \times 1 \times 0.1$ mm grown by a high-pressure flux method ([7]). Na-CCOC is devoid of complications such as superlattice modulations, bilayer splitting, and orthorhombic distortions and is highly 2D with a resistivity anisotropy ρ_c/ρ_{ab} of 10^4 ([8]). The x = 0.10 and 0.12 samples had T_c's of 13 and 22 K, respectively (maximum T_c = 28 K), whereas the x = 0.05 composition was nonsuperconducting. Typical energy and momentum resolutions were 14 meV and 0.35° (corresponding to $\Delta k \sim 0.02\ \pi/a_0$), and samples were measured at pressures lower than 5×10^{-11} torr.

In Fig. 1, A to C, we show the momentum distribution of spectral weight within a ± 10-meV window around the Fermi energy, E_F. The predominance of the nodal states can be seen in the raw data, as the intensity is maximum along the $(0,0)$-(π,π) nodal direction and drops off rapidy toward $(\pi,0)$, the anti-node. To better quantify the Fermi surface (FS), we have taken the maximal position in each momentum distribution curve (MDC) at E_F, which intersected the FS and identified this as a Fermi wave vector, $\mathbf{k}_F$. To minimize the effects of photoelectron matrix elements or sample-dependent variations, we confirmed our results on additional samples by varying photon energies (between 16.5 and 28 eV) or acquiring data with polarizations parallel to the Cu-O bond direction, or in the second Brillouin zone. All results are summarized in Fig. 1, D to F, and representative MDCs are overlaid in Fig. 1E. Despite the much weaker intensity of the antinodal MDC, its momentum structure nevertheless allows one to define $\mathbf{k}_F$ and establish a continuous contour reminiscent of the predicted noninteracting FS ([9]). Although this approach is robust in extracting the normal-state FS for conventional metallic or even gapped systems, the situation is less clear for strongly correlated systems where the quasi-particle (QP) residue, Z, can be much less than 1. However, we will still refer colloquially to these extracted contours as Fermi surfaces throughout this work ([10]).

The manifestation of the 2DCO in the ARPES spectra can be observed in Fig. 1, D to F, where the weak antinodal segments appear to be well nested and separated by approximately $|\mathbf{q}| \sim 2\pi/4a_0$ (Fig. 2A). In Fig. 2, A and B, we compare a schematic of the low-energy intensity with the real space dI/dV map ([6]). This correspondence is exhibited not only in the wave vectors, but also in the unusual energy (ω) dependence of this pattern. The tunneling data exhibit a surprising bias independence ([6]), and our antinodal MDCs (Fig. 2C) also demonstrate a similar insensitivity to ω below 50 meV, in contrast to the dispersive nodal MDCs (Fig. 2D). This unphysical vertical dispersion of the antinodal excitations is highly atypical and almost certainly does not represent the behavior of the actual QP band, as will be discussed later. The doping dependence of the nodal and antinodal $\mathbf{k}_F$'s is summarized in Fig. 2E. The relatively weak doping and ω dependence of the antinodal $\mathbf{k}_F$ is in stark contrast to the expected behavior of a near-E_F van Hove singularity, where both the doping and ω dependence of the MDCs should be sizable. Moreover, the contrast between the strong nodal states and weak antinodal segments is surprising given that the low-energy STM spectra are almost entirely dominated by the commensurate 2DCO ([6]).

This anisotropy can also be observed in the energy distribution curves (EDCs) along the

Fig. 1. (**A** to **C**) The momentum distribution of spectral weight within a ± 10-meV window around E_F for x = 0.05, 0.10, and 0.12 in one quadrant of the first Brillouin zone. Data were taken at 15 K with $h\upsilon$ = 25.5 eV and a polarization 45° to the Cu-O bond, normalized to a featureless background at high binding energies (-1 eV), and symmetrized along the $(0,0)$-(π,π) line. The data acquisition range is shown within the black

lines. The FS contours shown in (**D** to **F**) were compiled from more than four samples for each composition with photon energies between 16.5 and 28 eV and photon polarizations both parallel to and at 45° to the Cu-O bond direction. Data from these samples constitute the individual points; the best fit is shown as a solid line. The region in which a low-energy peak was typically observed is marked by gold circles. The gray shaded areas in (E) represent the momentum distribution of intensity at EF ± 10 meV along the $(0,0)$-(π,π) and $(\pi,0)$-(π,π) high-symmetry directions.
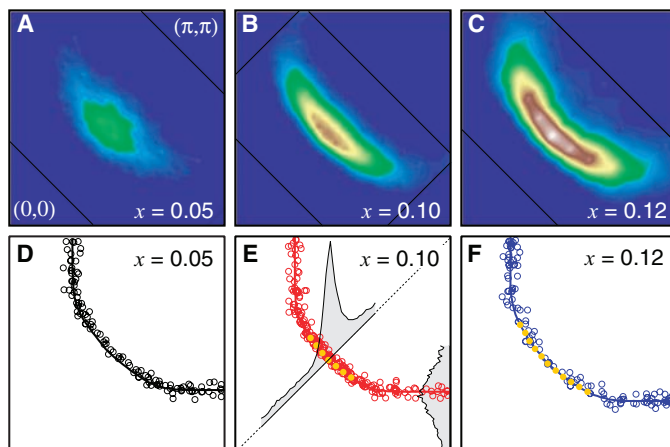
Fig. 2. (**A**) Schematic of the low-lying spectral intensity for x = 0.10. The hatched regions show the nested portions of FS, and the FS angle is defined in the lower right quadrant. (**B**) An STM dI/dV map from ([6]) is shown from $Ca_{1.9}Na_{0.1}CuO_2Cl_2$, taken at 24 meV and 100 mK, exhibiting the $4a_0 \times 4a_0$ ordering. MDCs along the antinodal (**C**) and nodal (**D**) directions are shown for $Ca_{1.88}Na_{0.12}CuO_2Cl_2$, taken at 15 K with $h\upsilon$ = 25.5 eV. (**E**) The doping dependence of the $\mathbf{k}_F$ wave vectors along the $(0,0)$-(π,π) (blue triangles) and $(\pi,0)$-(π,π) (red circles) directions. Error bars show the SD from sample to sample.
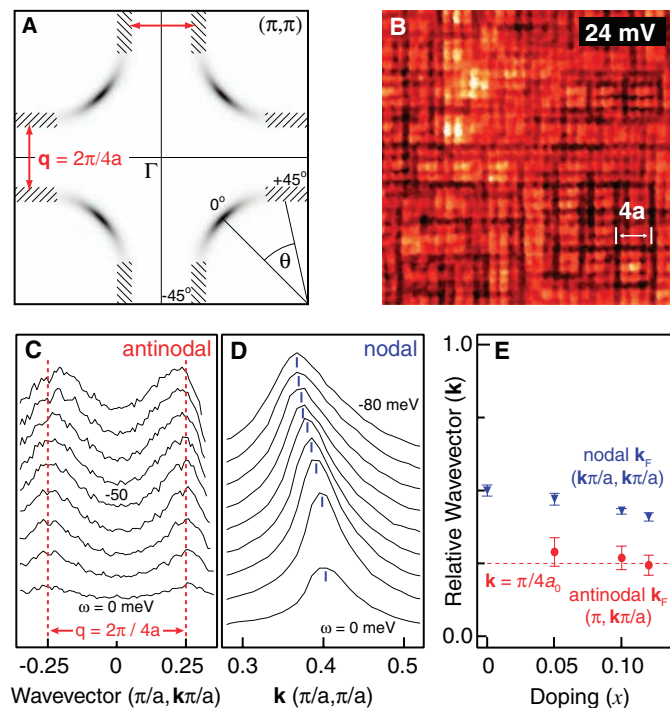
FS (Fig. 3A). At $x = 0.10$ and 0.12, sharp peaks in the EDCs are observed only near the nodal direction, whereas the antinodes exhibit a depletion of spectral weight over a wide energy range (~200 meV), a phenomenon observed in underdoped cuprates including $Bi_2Sr_2CaCu_2O_{8+\delta}$, $La_{2-x}Sr_xCuO_4$, and Na-CCOC, often referred to as a high-energy pseudogap (11). From the EDCs in Fig. 3A, it is clear that the intensity anisotropy in Fig. 1, A to C, is not due simply to the opening of a d-wave superconducting (SC) gap, where Bogoliubov QPs should remain well defined over the entire Brillouin zone. In fact, no substantial changes in the spectra were observed upon cooling or warming the samples through T_c (between 10 and 50 K), unlike the cases of near-optimally doped $Bi_2Sr_2CaCu_2O_{8+\delta}$ (12) or $YBa_2Cu_3O_{7-\delta}$ (13), in which a coherent peak emerges in the antinodal regions below T_c. The absence of any marked change may be associated with the low T_c or the doping level, given that SC antinodal peaks are also absent in underdoped $La_{2-x}Sr_xCuO_4$ and $Bi_2Sr_2CuO_{6+\delta}$ (11, 14, 15). However, a slight leading-edge gap of the antinodal spectra is observed [8 ± 4 meV for $x = 0.10$, 7 ± 4 meV for $x = 0.12$ (errors are determined from fitting and sample-to-sample variations)], consistent with a low-energy pseudogap. These values are quite consistent with the leading edge gap values observed in compounds with comparable T_c's, such as $La_{2-x}Sr_xCuO_4$ or $Bi_2Sr_2CuO_{6+\delta}$ (11, 14, 15), whereas they are substantially smaller than in $Bi_2Sr_2CaCu_2O_{8+\delta}$ (11), which has a much higher T_c.
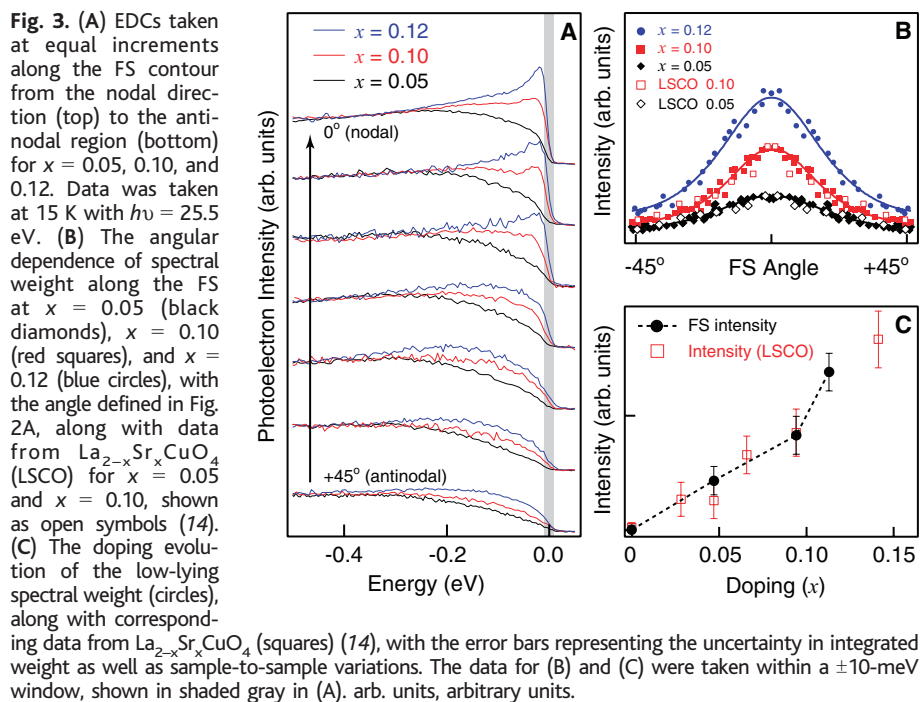
In conventional charge-density wave (CDW) systems, nesting of the FS gives rise to a divergent Lindhard susceptibility that results in a Peierls instability. The formation of the CDW results in a larger unit cell and a folding of the original bands, but coherent QPs still exist, as demonstrated by ARPES studies of quasi–2D CDW systems such as $CeTe_3$ (16) or In/Cu(001) (17). Therefore, the seemingly incoherent antinodal features cannot be produced from FS nesting or ordering alone, so additional factors must be considered. Along these lines, the antinodal spectra from Na-CCOC bear close resemblance to data from $La_{1.2}Sr_{1.8}Mn_2O_7$, in which a similar high-energy pseudogap was observed on portions of the FS that have a nesting wave vector corresponding to CDW ordering (18). In this case, the high-energy pseudogap was attributed to the coupling of the electrons to Jahn-Teller distortions of the MnO_6 octahedra, which are believed to play a critical role in the low-energy electronic properties of the manganites, because the Mn^{4+} ions are in a d^3 configuration with unoccupied orbitals of e_g symmetry (19). Although the detailed microscopic interactions in the cuprates and manganites are rather different, the two systems may still share a similar general phenomenology.

In Fig. 3B, we show the doping evolution of the low-energy spectral weight associated with the FS and Z, where the intensity increases monotonically as a function of doping, behavior unexpected in simple one-electron pictures. This was confirmed by normalizing all MDCs and spectra at all dopings to either the flat high-energy spectra at ~–1 eV or to features in the valence band (–2 to –7 eV), both of which were largely doping independent. Although it appears from Fig. 1, A to C, that the FS elongates toward the antinodes with increasing doping, this effect is illusory and arises simply from the overall increase in intensity, as the shape of the angular distribution of spectral weight does not change appreciably with doping. This suggests that Z and the self-energy retain a qualitatively similar $\mathbf{k}$ anisotropy throughout the underdoped regime.

The absence of sharp antinodal excitations, the doping-dependent growth of low-energy weight, and the $\mathbf{k}$ anisotropy of FS intensity in Na-CCOC all demonstrate marked resemblances to measurements from lightly doped $La_{2-x}Sr_xCuO_4$ (14, 15). This is shown in Fig. 3, B and C, in which data from $La_{2-x}Sr_xCuO_4$ (14) are overlaid onto data from Na-CCOC and scaled to match either the nodal intensity at the same compositions (Fig. 3B) or the general doping trends (Fig. 3C). These similarities suggest an intrinsic commonality between the low-lying excitations across different cuprate families and may imply a generic microscopic origin for these essential nodal states irrespective of other ordering tendencies. At very low doping levels, the nodal excitations should entirely dominate the transport properties, consistent with

the high-temperature metallic tendencies observed in very lightly doped cuprates (20). Thus any microscopic models of charge ordering must also simultaneously explain and incorporate the existence of coherent nodal states and broad antinodal excitations as essential features of the single-particle excitation spectrum. In addition, similar faint and nested antinodal FS segments have been observed by ARPES in $La_{2-x}Sr_xCuO_4$ (15) and could correspond to an analogous 2D charge-ordered state. However, ARPES is a macroscopically averaged probe and cannot distinguish between true 2D ordering and a superposition of 1D domains. Despite the qualitative similarities between the low-energy features of $La_{2-x}Sr_xCuO_4$ and Na-CCOC, there exist important quantitative differences that could potentially be detected by future STM experiments, including the considerably smaller high-energy pseudogap and antinodal wave vector in $La_{2-x}Sr_xCuO_4$ at comparable doping levels (e.g., $|\mathbf{q}| \sim 0.35\ \pi/a_0$ for $x = 0.063$) (11, 14, 15).

In addition, the identification of similar charge modulation patterns by STM in another compound, $Bi_2Sr_2CaCu_2O_{8+\delta}$, also suggests the possible universality of electronic ordering in all cuprates. Electronic checkerboard patterns are evident in $Bi_2Sr_2CaCu_2O_{8+\delta}$ when SC is destroyed [above T_c (21), inside vortex cores (22)] or in very underdoped samples (23) and may be associated with the absence of sharp antinodal SC excitations in many cuprates studied by ARPES at low doping levels [such as Na-CCOC and $La_{2-x}Sr_xCuO_4$ (14, 15)] or above T_c in underdoped materials [such as $Bi_2Sr_2CaCu_2O_{8+\delta}$ (11)]. Although many

Fig. 3. (A) EDCs taken at equal increments along the FS contour from the nodal direction (top) to the antinodal region (bottom) for $x = 0.05$, 0.10, and 0.12. Data was taken at 15 K with $h\upsilon = 25.5$ eV. (B) The angular dependence of spectral weight along the FS at $x = 0.05$ (black diamonds), $x = 0.10$ (red squares), and $x = 0.12$ (blue circles), with the angle defined in Fig. 2A, along with data from $La_{2-x}Sr_xCuO_4$ (LSCO) for $x = 0.05$ and $x = 0.10$, shown as open symbols (14). (C) The doping evolution of the low-lying spectral weight (circles), along with corresponding data from $La_{2-x}Sr_xCuO_4$ (squares) (14), with the error bars representing the uncertainty in integrated weight as well as sample-to-sample variations. The data for (B) and (C) were taken within a ±10-meV window, shown in shaded gray in (A). arb. units, arbitrary units.

particular details of the 2DCO state may be material dependent, there appears to be a general correspondence between the broad and nested antinodal FS segments observed by ARPES and the propensity for 2D charge ordering in the lightly doped cuprates.

One recent intriguing model proposed for the 2DCO is a Wigner crystal (WC), whose formation is driven by the Coulomb repulsion between the doped holes (*24*). Although 2D WCs or 1D stripes provide appealing real-space visualizations, addressing the nodal states in a fundamental manner may prove difficult for these models. For the simple WC picture, virtually all holes should be locked into an insulating superlattice and the low-energy QPs arise from the overflow or deficit of holes away from certain favored commensurate dopings. On the other hand, in $La_{2-x}Sr_xCuO_4$ it has been argued that the nodal states may arise from disordered stripes (*25*). In both cases, the nodal states arise more as model-dependent byproducts, not fundamental constituents of the charge-ordered state.

On the other hand, it has long been known that CDW formation and SC are competing instabilities in a wide variety of materials (*26*). This is not entirely surprising, given that the same attractive effective interactions, typically electron-phonon, can give rise to both states in many materials. In the case of Na-CCOC, both *d*-SC and 2DCO appear to compete for the antinodes, and the strength of one order parameter should come at the expense of the other. For instance, although $Ca_{2-x}Na_xCuO_2Cl_2$ is a rather poor high-T_c SC, it exhibits very prominent modulations in the STM dI/dV maps. On the other hand, $Bi_2Sr_2CaCu_2O_{8+\delta}$ is one of the better high-T_c superconductors (maximum $T_c = 96$ K), but exhibits far less pronounced charge-density modulations at low energies (*21–23*). Along these lines, it is also possible that critical fluctuations between the 2DCO and another ordered state could result in the incoherent antinodal states (*27*), although it is not evident whether the nodal QPs would still remain well defined. A related possibility is that the 2DCO does not represent a CDW of single holes, but instead represents a density wave of preformed *d*-wave Cooper pairs or a pair density wave (PDW) (*28*).

Another potential explanation for the broad antinodal features may come from models based on Franck-Condon broadening, which have been proposed to describe the unusual spectral features in both the lightly doped cuprates (*29*, *30*) and the manganites (*31*), and may therefore explain the similarity of the high-energy pseudogaps found in the both systems. In such a scenario, the strong coupling of the electrons to any bosonic excitations would result in $Z \ll 1$, and spectral weight is transferred to in-

coherent, multiboson excitations. The high-energy pseudogap behavior in both the cuprates and manganites may then originate from the broad, suppressed tail of incoherent spectral weight, which obscures the very small, but possibly finite coherent QP. The apparently vertical dispersion in the anti-nodal regime can then be explained as originating not from a real QP band, but rather from this largely incoherent, pseudo-gapped spectral weight. In this picture, an effective anisotropic coupling could lead to a larger Z (weaker coupling) along the nodal direction and a much smaller, yet still finite Z, at the antinodes (strong coupling). However, this coupling alone may not be sufficient to cause the 2DCO, and it may be the combination of strong coupling and FS nesting which ultimately stabilizes the antinodal charge-ordered state.

Although Na-CCOC may provide the clearest case for relating real-space charge ordering to the anisotropy of electronic states in momentum space, we believe that this is indicative of a generic tendency of the cuprate superconductors. Irrespective of the microscopic model, the dichotomy between the sharp nodal QPs and broad antinodal states suggests the importance of strongly momentum-anisotropic interactions in Na-CCOC and places important restrictions on possible theoretical descriptions of the charge-ordered state and pseudogap phase.

References and Notes
1. T. Timusk, B. Statt, *Rep. Prog. Phys.* **62**, 61 (1999).
2. I. Affleck, J. B. Marston, *Phys. Rev. B* **37**, 3774 (1988).
3. J. Zaanen, O. Gunnarsson, *Phys. Rev. B* **40**, 7391 (1989).
4. J. M. Tranquada *et al.*, *Nature* **375**, 561 (1995).
5. V. J. Emery, S. A. Kivelson, H. Q. Lin, *Phys. Rev. Lett.* **64**, 475 (1990).
6. T. Hanaguri *et al.*, *Nature* **430**, 1001 (2004).
7. Y. Kohsaka *et al.*, *J. Am. Chem. Soc.* **124**, 12275 (2002).
8. K. Waku *et al.*, *Phys. Rev. B* **70**, 134501 (2004).
9. L. F. Mattheiss, *Phys. Rev. B* **42**, 354 (1990).
10. The observed discrepancy between the nominal Na composition and the area enclosed in the contours shown in Fig. 1, C and D, could imply that the experimentally extracted contours may not represent a true FS in the strict Fermi liquid sense, possibly because of the broad antinodal excitations.
11. A. Damascelli, Z. Hussain, Z.-X. Shen, *Rev. Mod. Phys.* **75**, 473 (2003).
12. D. S. Dessau *et al.*, *Phys. Rev. Lett.* **66**, 2160 (1991).
13. D. H. Lu *et al.*, *Phys. Rev. Lett.* **86**, 4370 (2001).
14. T. Yoshida *et al.*, *Phys. Rev. Lett.* **91**, 027001 (2003).
15. X. J. Zhou *et al.*, *Phys. Rev. Lett.* **92**, 187001 (2004).
16. V. Brouet *et al.*, *Phys. Rev. Lett.* **93**, 126405 (2004).
17. T. Nakagawa *et al.*, *Phys. Rev. B* **67**, 241401 (2003).
18. Y.-D. Chuang, A. D. Gromko, D. S. Dessau, T. Kimura, Y. Tokura, *Science* **292**, 1509 (2001).
19. M. B. Salamon, M. Jaime, *Rev. Mod. Phys.* **73**, 583 (2001).
20. Y. Ando, A. N. Lavrov, S. Komiya, K. Segawa, X. F. Sun, *Phys. Rev. Lett.* **87**, 017001 (2001).
21. M. Vershinin *et al.*, *Science* **303**, 1995 (2004).
22. J. E. Hoffman *et al.*, *Science* **295**, 466 (2002).
23. K. McElroy *et al.*, in preparation; preprint available at http://arxiv.org/cond-mat/0404005.
24. H. C. Fu, J. C. Davis, D.-H. Lee, in preparation; preprint available at http://arxiv.org/cond-mat/0403001.
25. M. I. Salkola, V. J. Emery, S. A. Kivelson, *Phys. Rev. Lett.* **77**, 155 (1996).
26. A. M. Gabovich, A. I. Voitenko, J. F. Annett, M. Ausloos, *Supercond. Sci. Technol.* **14**, R1 (2001).
27. S. Sachdev, *Science* **288**, 475 (2000).
28. H.-D. Chen, O. Vafek, A. Yazdani, S.-C. Zhang, *Phys. Rev. Lett.* **93**, 187002 (2004).
29. A. S. Mishchenko, N. Nagaosa, *Phys. Rev. Lett.* **93**, 036402 (2004).
30. K. M. Shen *et al.*, *Phys. Rev. Lett.* **93**, 267002 (2004).
31. V. Perebeinos, P. B. Allen, *Phys. Rev. Lett.* **85**, 5178 (2000).
32. We thank N. P. Armitage, H.-D. Chen, A. Damascelli, J. C. Davis, T. P. Devereaux, H. Eisaki, T. Hanaguri, J. P. Hu, D.-H. Lee, N. Nagaosa, T. Sasagawa, O. Vafek, S. C. Zhang, and X. J. Zhou for enlightening discussions. Stanford Synchrotron Radiation Laboratory is operated by the Department of Energy Office of Basic Energy Science under contract DE-AC03-765F00515. K.M.S. acknowledges Stanford Graduate Fellowships and Natural Sciences and Engineering Research Council of Canada for their support. The ARPES measurements at Stanford were also supported by NSF DMR-0304981 and Office of Naval Research N00014-98-1-0195.

Asynchronous Bends in Pacific Seamount Trails: A Case for Extensional Volcanism?

Anthony A. P. Koppers* and Hubert Staudigel

The Gilbert Ridge and Tokelau Seamounts are the only seamount trails in the Pacific Ocean with a sharp 60° bend, similar to the Hawaii-Emperor bend (HEB). These two bends should be coeval with the 47-million-year-old HEB if they were formed by stationary hot spots, and assuming Pacific plate motion only. New $^{40}Ar/^{39}Ar$ ages indicate that the bends in the Gilbert Ridge and Tokelau seamount trail were formed much earlier than the HEB at 67 and 57 million years ago, respectively. Such asynchronous bends cannot be reconciled with the stationary hot spot paradigm, possibly suggesting hot spot motion or magmatism caused by short-term local lithospheric extension.

The Hawaii-Emperor island and seamount chain is the most prominent morphologic feature on the seafloor, with a sharp 60° change

in azimuth, called the Hawaii-Emperor bend (HEB). The HEB serves as a textbook example of the fixed hot spot hypothesis, in